Structure of bone morphogenetic protein 9 procomplex

Li-Zhi Mi[a,b,c], Christopher T. Brown[d], Yijie Gao[d], Yuan Tian[a,b], Viet Q. Le[a,b], Thomas Walz[e,f], and Timothy A. Springer[a,b,1]

[a]Department of Biological Chemistry and Molecular Pharmacology, Harvard Medical School, Boston, MA 02115; [b]Program in Cellular and Molecular Medicine, Children's Hospital Boston, Boston, MA 02115; [c]Department of Molecular and Structural Biology, School of Life Sciences, Tianjin University, Tianjin 300072, China; [d]Global BioTherapeutics Technologies, Pfizer Worldwide Research and Development, Cambridge, MA 02139; and [e]Howard Hughes Medical Institute and [f]Department of Cell Biology, Harvard Medical School, Boston, MA 02115

Contributed by Timothy A. Springer, January 27, 2015 (sent for review January 2, 2015; reviewed by Daniel Rifkin and Lynn Y. Sakai)

Bone morphogenetic proteins (BMPs) belong to the TGF-β family, whose 33 members regulate multiple aspects of morphogenesis. TGF-β family members are secreted as procomplexes containing a small growth factor dimer associated with two larger prodomains. As isolated procomplexes, some members are latent, whereas most are active; what determines these differences is unknown. Here, studies on pro-BMP structures and binding to receptors lead to insights into mechanisms that regulate latency in the TGF-β family and into the functions of their highly divergent prodomains. The observed open-armed, nonlatent conformation of pro-BMP9 and pro-BMP7 contrasts with the cross-armed, latent conformation of pro-TGF-β1. Despite markedly different arm orientations in pro-BMP and pro-TGF-β, the arm domain of the prodomain can similarly associate with the growth factor, whereas prodomain elements N- and C-terminal to the arm associate differently with the growth factor and may compete with one another to regulate latency and stepwise displacement by type I and II receptors. Sequence conservation suggests that pro-BMP9 can adopt both cross-armed and open-armed conformations. We propose that interactors in the matrix stabilize a cross-armed pro-BMP conformation and regulate transition between cross-armed, latent and open-armed, nonlatent pro-BMP conformations.

Members of the TGF-β family including bone morphogenetic proteins (BMPs) are biosynthesized and processed into complexes between large prodomains and smaller, C-terminal mature growth factor (GF) domains that are separated by proprotein convertase (PC) (furin) cleavage sites. In the original isolation of proteins responsible for BMP activity, bone was first demineralized with 0.5 M HCl. The resulting residual matrix was extracted with 6 M urea or 4 M guanidine HCl (1–3). During subsequent purification under largely denaturing conditions, the GF domains were separated from their prodomains. Therefore, little attention was paid to the potential existence of BMP procomplexes. However, evidence exists that BMP prodomains contribute to maintaining BMP GF domains inactive or latent in vivo. For example, early studies showed a 60-fold increase in total BMP activity during the first two purification steps following extraction of the BMP, which was interpreted as purification of BMP away from an inhibitor (2). This finding is consistent with the presence of largely latent complexes between BMPs, their prodomains, and extracellular matrix components in the insoluble residual matrix from which BMPs were purified. In agreement with a regulatory role for the prodomain, mutations of secondary PC sites within the prodomain perturb embryonic development in insects and vertebrates, suggesting that prodomains of several BMPs remain associated with GFs after secretion and regulate the distance over which BMPs signal (4–7). An important role for the prodomain in development is also illustrated by prodomain mutations, including in secondary PC cleavage sites, that cause human diseases (5, 7).

Pro-TGF-β is latent; however, when overexpressed as recombinant proteins, most BMPs are active. Although noncovalently associated with their GF after secretion, the prodomains of most BMPs do not bind strongly enough to prevent GF from binding to receptors and signaling (8, 9). To better understand such differences among members of the TGF-β family, we examine the structure of pro-BMP9 and compare it to the previously described, cross-armed conformation of pro-TGF-β1 (10). Although a member of the BMP subfamily and possessing chondrogenic and osteogenic activity, BMP9 is expressed in liver and is required for properly organized blood and lymphatic vascular development (11, 12). Mutations in the prodomain of BMP9, in its receptor Alk1, and in its coreceptor endoglin cause phenotypically overlapping hereditary hemorrhagic telangiectasias (13–15).

Here, we reveal surprising open-armed conformations of pro-BMPs 7 and 9. We propose that binding to interactors in the matrix may regulate transition between open-armed and cross-armed conformations in the TGF-β family and that these conformations regulate GF latency.

Results

Structures of BMP Procomplexes. In marked contrast to the cross-armed, ring-like conformation of pro-TGF-β1 (10), crystal structures of natively glycosylated pro-BMP9 reveal an unexpected, open-armed conformation (Fig. 1 *A* and *B* and Table S1). All negative stain EM class averages show an open-armed conformation for pro-BMP9 (Fig. 1*C* and Fig. S1) and a similar, although less homogenous, open-armed conformation for pro-BMP7 (Fig. 1*D* and Fig. S2). Crystal structure experimental electron density is excellent (Fig. S3) and allows us to trace the complete structure of each pro-BMP9 arm domain (residues 63–258; Fig. 1*E*). As in pro-TGF-β1, the arm domain has two β-sheets that only partially overlap. Hydrophobic, nonoverlapping portions of the β-sheets are covered by meandering loops and the α4-helix (Fig. 1 *E* and *F*). Comparison of pro-BMP9 and pro-TGF-β1 arm domains defines a conserved core containing two four-stranded β-sheets and the α4-helix (labeled in black in Fig. 1 *E* and *F*).

One of the BMP9 arm domain β-sheets joins a finger-like β-sheet in the GF to form a super β-sheet (Fig. 1 *A* and *G*). Each GF monomer has a hand-like shape. The two BMP9 GF hands

Significance

Bone morphogenetic protein (BMP) activity is regulated by prodomains. Here, structures of BMP procomplexes reveal an open-armed conformation. In contrast, the evolutionarily related, latent TGF-β1 procomplex is cross-armed. We propose that in the TGF-β and BMP family, conversion between cross-armed and open-armed conformations may regulate release and activity of the growth factor.

Author contributions: T.A.S. designed research; L.-Z.M., C.T.B., Y.G., Y.T., V.Q.L., T.W., and T.A.S. performed research; L.-Z.M., C.T.B., Y.G., Y.T., V.Q.L., T.W., and T.A.S. analyzed data; and L.-Z.M., C.T.B., Y.T., V.Q.L., and T.A.S. wrote the paper.

Reviewers: D.R., NYU Langone Medical Center; and L.Y.S., Shriners Hospitals for Children.

The authors declare no conflict of interest.

Data deposition: The atomic coordinates and structure factors have been deposited in the Protein Data Bank, www.pdb.org (PDB ID codes 4YCG and 4YCI).

[1]To whom correspondence should be addressed. Email: timothy.springer@childrens.harvard.edu.

This article contains supporting information online at www.pnas.org/lookup/suppl/doi:10.1073/pnas.1501303112/-/DCSupplemental.

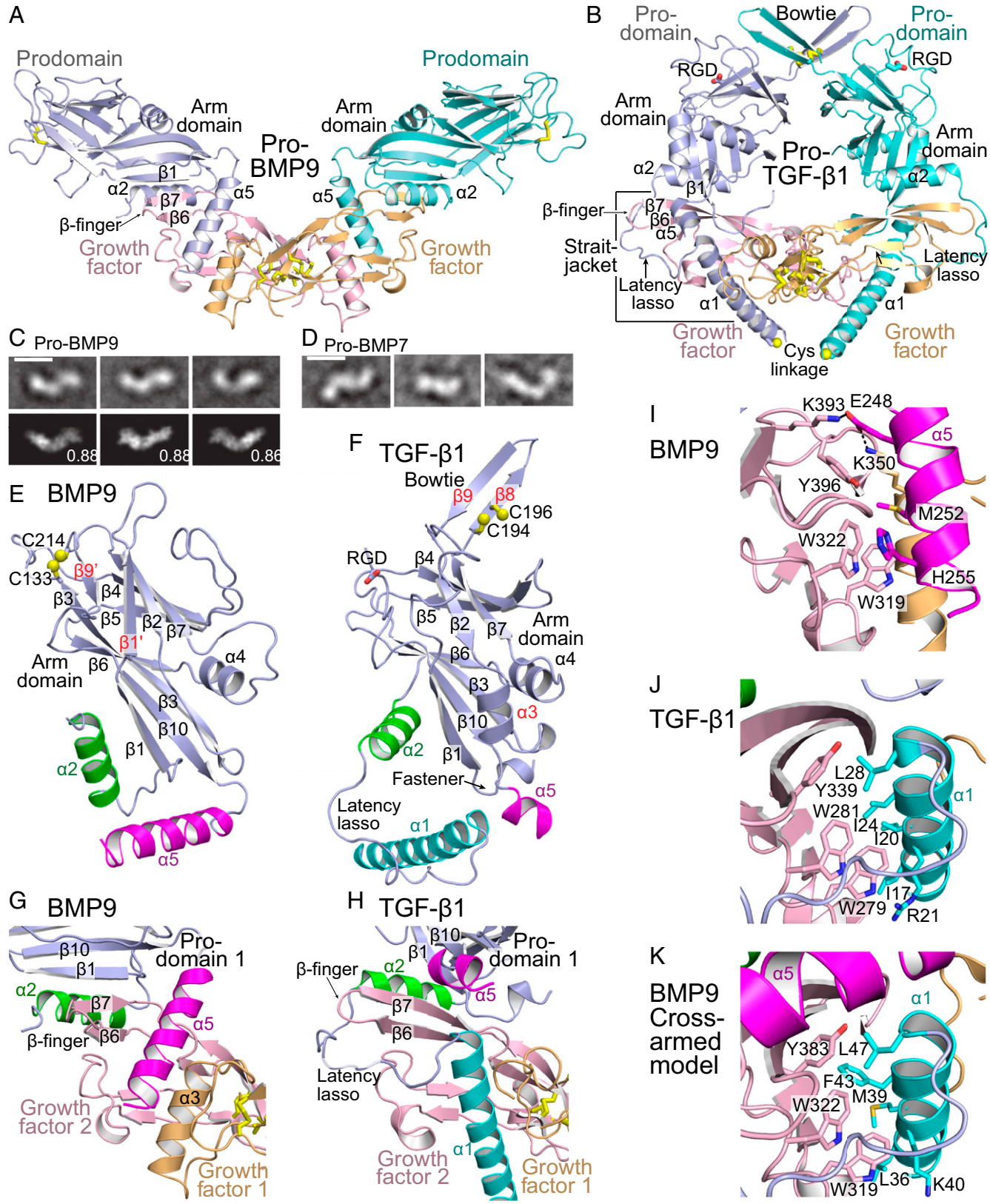

Fig. 1. Structures. (*A* and *B*) Cartoon diagrams of pro-BMP9 (*A*) and pro-TGF-β1 (10) (*B*) with superimposition on GF dimers. Disulfides (yellow) are shown in stick. (*C* and *D*) Representative negative-stain EM class averages of pro-BMP9 (*C*) and pro-BMP7 (*D*). Best correlating projections of the pro-BMP9 crystal structure with their normalized cross-correlation coefficients are shown below class averages. (Scale bars, 100 Å.) (*E* and *F*) BMP9 and TGF-β1 prodomains shown in cartoon after superimposition. Core arm domain secondary structural elements are labeled in black and others in red. Helices that vary in position between cross- and open-armed conformations are color-coded. Spheres show Cys S atoms. (*G*–*K*) Prodomain–GF interactions in pro-BMP9 (*G* and *I*), pro-TGF-β1 (*H* and *J*), and a model of cross-armed pro-BMP9 (*K*). Structures are superimposed on the GF monomer. Colors are as in *A, B, E*, and *F*. Key residues are shown in stick.

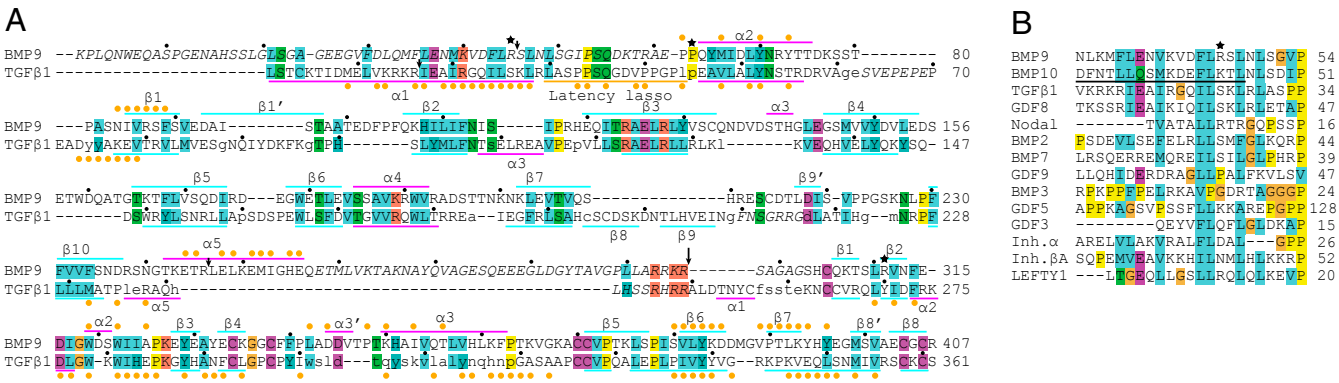

Fig. 2. Sequence alignments. (*A*) Sequences aligned structurally with SSM (26). Structurally aligned residues are in uppercase; lowercase residues are not structurally aligned. Residues with missing density are in italics. Decadal residues are marked with black dots. Residues with more than 50% solvent accessible surface area buried in prodomain–GF interfaces are marked with gold dots. Secondary structural elements or named regions are shown with lines. Long black arrow marks cleavage sites between the prodomain and GF; short black arrows mark putative PC cleavage sites after the α1-helix and in the α5-helix. Stars mark HHT-like mutation sites. (*B*) Sequence alignment of representative TGF-β family members in the prodomain α1-helix (overlined for TGF-β1).

dimerize in their palm regions (Fig. 1*A* and Fig. S4) in an interface that buries 1,280 Å^2 of solvent-accessible surface.

The interface between each BMP9 prodomain and GF monomer buries 1,440 Å^2. The larger size of the prodomain–GF interface than the GF–GF interface emphasizes its significance, as does the super β-sheet interface between the prodomain and GF and the burial of hydrophobic residues by this interface and by the prodomain α2-helix (Fig. 1*A*). A specialization in pro-BMP9 not present in pro-TGF-β1 is a long α5-helix (Fig. 1 *A*, *B*, *E*, and *F*) that is a C-terminal appendage to the arm domain and that separately interacts with the GF dimer to bury 750 Å^2 (Fig. 1*A*).

Despite markedly different arm domain orientations, topologically identical secondary structure elements form the interface between the prodomain and GF in pro-BMP9 and pro-TGF-β1: the β1-strand and α2-helix in the prodomain and the β6- and β7-strands in the GF (Fig. 1 *A*, *B*, *G*, and *H*). The outward-pointing, open arms of pro-BMP9 have no contacts with one another, which results in a monomeric prodomain–GF interaction. In contrast, the inward pointing arms of pro-TGF-β1 dimerize through disulfides in their bowtie motif, resulting in a dimeric, and more avid, prodomain-GF interaction (Fig. 1 *A* and *B*).

Twists at two different regions of the interface result in the remarkable difference in arm orientation between BMP9 and TGF-β1 procomplexes. The arm domain β1-strand is much more twisted in pro-TGF-β1 than in pro-BMP9, enabling the β1-β10-β3-β6 sheets to orient vertically in pro-TGF-β and horizontally in pro-BMP9 in the view of Fig. 1 *A* and *B*. In addition, if we imagine the GF β7- and β6-strands as forefinger and middle finger, respectively, in BMP9, the two fingers bend inward toward the palm, with the β7 forefinger bent more, resulting in cupping of the fingers (Fig. 1 *G* and *H* and Fig. S4). In contrast, in TGF-β1, the palm is pushed open by the prodomain amphipathic α1-helix, which has an extensive hydrophobic interface with the GF fingers and inserts between the two GF monomers (Fig. 1*B*) in a region that is remodeled in the mature GF dimer and replaced by GF monomer–monomer interactions (10).

Role of Elements N and C Terminal to the Arm Domain in Cross- and Open-Armed Conformations. A straitjacket in pro-TGF-β1 composed of the prodomain α1-helix and latency lasso encircles the GF on the side opposite the arm domain (Fig. 1*B*). Sequence for putative α1-helix and latency lasso regions is present in pro-BMP9 (Fig. 2*A*); however, we do not observe electron density corresponding to this sequence in the open-armed pro-BMP9 map. Furthermore, in the open-armed pro-BMP9 conformation, the prodomain α5-helix occupies a position that overlaps with the position of the α1-helix in the cross-armed pro-TGF-β1 conformation (Fig. 1 *A*, *B*, *G*, and *H*). The differing twists between the arm domain and GF domains in open-armed and cross-armed conformations relate to the distinct ways in which the prodomain α5-helix in pro-BMP9 and the α1-helix in pro-TGF-β1 bind to the GF (Fig. 1 *A* and *B*). The strong sequence signature for the α1-helix in pro-BMP9, which is essential for the cross-armed conformation in pro-TGF-β, suggests that pro-BMP9 can also adopt a cross-armed conformation (*Discussion*).

In absence of interaction with a prodomain α1-helix, the GF dimer in pro-BMP9 is much more like the mature GF (1.6-Å RMSD for all Cα atoms) than in pro-TGF-β1 (6.6-Å RMSD; Fig. S4). Moreover, burial between the GF and prodomain dimers is less in pro-BMP9 (2,870 Å^2) than in pro-TGF-β1 (4,320 Å^2). In the language of allostery, GF conformation is tensed in cross-armed pro-TGF-β1 and relaxed in open-armed pro-BMP9.

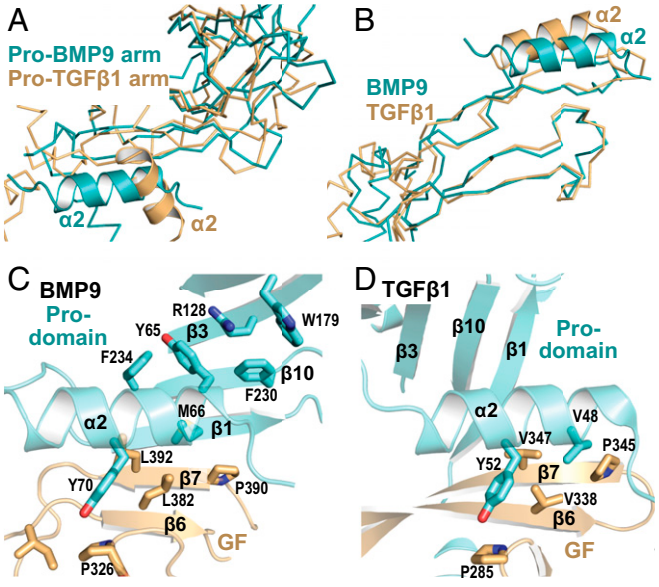

Fig. 3. The prodomain α2-helix. (*A* and *B*) Superimpositions based on the arm domain (*A*) or on the GF (*B*), which are shown as Cα traces with the α2-helix in cartoon. (*C* and *D*) Prodomain α2-helix environments in pro-BMP9 (*C*) and pro-TGF-β1 (*D*) shown after superimposition on the prodomain α2-helix and GF β6 and β7-strands. Key interacting residues are shown in stick.

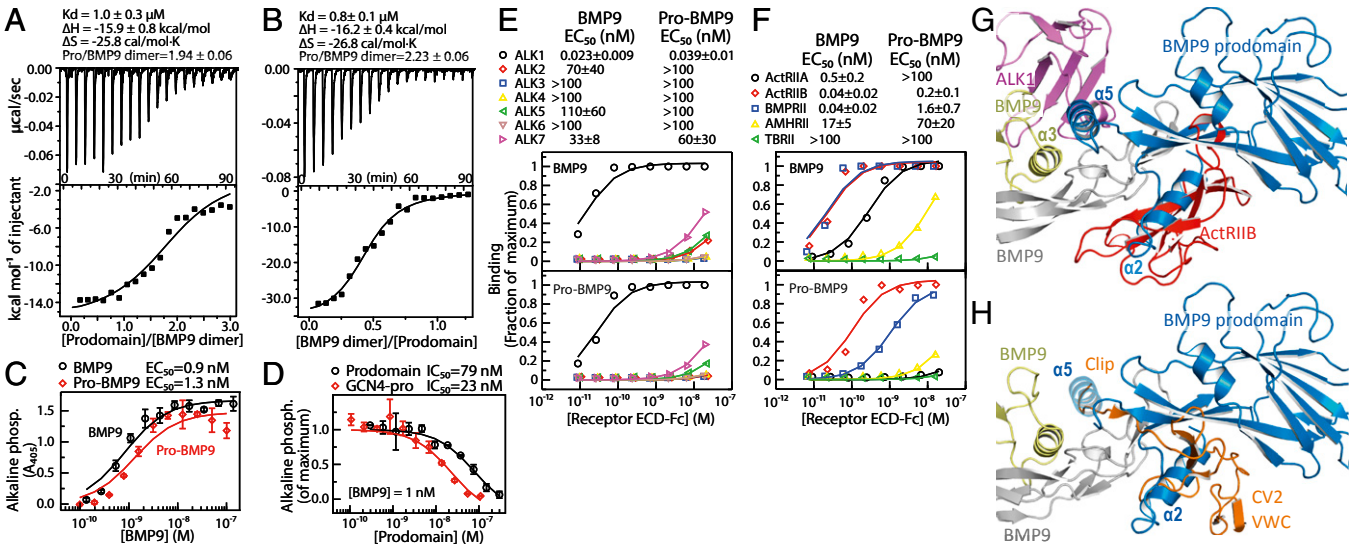

Fig. 4. Binding of BMP9 to the prodomain and receptors. (*A* and *B*) Representative ITC data at 15 °C adding material either to the BMP9 dimer (*A*) or prodomain (*B*) in the calorimetry cell. (*Upper*) Baseline-corrected raw data. (*Lower*) Integrated heats fit to the independent-binding site model. (*C* and *D*) Differentiation of C2C12 cells measured by alkaline phosphatase production. (*C*) Comparison of BMP9 and pro-BMP9. (*D*) Inhibition of 1 nM BMP9 by GCN4-linked, oligomeric BMP9 prodomain and native prodomain. (*E* and *F*) EC_{50} values of BMP9 and pro-BMP9 for Fc-fused type I (*E*) or type II (*F*) receptor ectodomains measured using quantitative ELISA. Data are plotted as the fraction of maximal bound in each experiment and fit to the equation of fractional saturation. Graphs show average of triplicates in one experiment; numerical values show mean EC_{50} and sd from three such experiments. (*G* and *H*) Superimpositions on pro-BMP9 of the BMP9–receptor complex (17) (*G*) and BMP2-crossveinless2 complex (*H*) in identical orientations. For clarity, BMP in receptor and inhibitor complexes is omitted, and the α5-helix is transparent in *H*.

The prodomain α2-helix covers the interface between the arm and GF domains and acts as a buffer between the open-armed and cross-armed conformations. With superimposition based on arm domains, α2-helix orientation differs by ∼90° in pro-BMP9 and pro-TGF-β1 (Figs. 1 *E* and *F* and 3*A*), whereas with superimposition based on GF monomers, α2-helix orientation is similar in pro-BMP9 and pro-TGF-β1 (Figs. 1 *G* and *H* and 3*B*). Thus, if we imagine shape-shifting between open- and cross-armed conformations of pro-BMP9 (*Discussion*), the α2-helix moves in harmony with the GF rather than the arm domain.

Prodomain α2-helix association with the GF is stabilized by conserved interactions. Homologous α2-helix residues Tyr-70 in pro-BMP9 and Tyr-52 in pro-TGF-β1 stack against homologous Pro-326 and Pro-285 residues in their GFs (Fig. 3 *C* and *D*). Moreover, homologous α2-helix residues Met-66 in pro-BMP9 and Val-48 in pro-TGFβ1 are buried in a hydrophobic cavity on their GFs (Fig. 3 *C* and *D*).

The α2-helix in open-armed pro-BMP9 interacts with the arm domain in a way not seen in cross-armed pro-TGF-β1. Tyr-65 from the α2-helix together with Trp-179 and Phe-230 from the arm domain form an aromatic cage (Fig. 3*C*). Arm residue Arg-128 at the center of this cage forms π–cation interactions with Tyr-65 and Trp-179 (Fig. 3*C*). Residues for the π-cation cage are well conserved in BMP4, 5, 6, 7, 8, and 10, GDF5, 6, and 7, and GDF15 (Fig. S5). However, in BMP2 and BMP15, Arg-128 is replaced by Gln, potentially weakening association of the prodomain with the GF in the open-armed conformation.

The similar arm domain cores and α2-helices in the prodomains of BMP9 and TGF-β1 are remarkable, given that the prodomains have only 11% identity in sequence and have 12 insertions/deletions (Fig. 2*A*). This contrasts with the 25% identity between their GF domains (Fig. 2*A*). Among notable differences, pro-BMP9 lacks the 14-residue bowtie in pro-TGF-β1 that disulfide links the two arm domains together and has in its place a β7-β9' loop (Fig. 2*A*). The two cysteine residues in the TGF-β1 arm domain, Cys-194 and Cys-196 (Fig. 1*F*), form reciprocal interchain disulfide bonds (10). In contrast, our pro-BMP9 structure shows that the two arm domain cysteines, Cys-133 and Cys-214, form an intrachain disulfide that links the β3 strand to the β7-β9' loop (Fig. 1*E*). The disulfide helps stabilize an extension of the β3-strand in BMP9 and the formation of the β1'- and β9'-strands unique to pro-BMP9 that add onto the β2-β7-β5-β4 sheet (Fig. 1 *E* and *F*).

The α5-helix in pro-BMP9 is its most surprising specialization. It is much longer than in pro-TGF-β1, orients differently (Fig. 1 *E* and *F*), and binds to a similar region of the GF domain as the α1-helix in pro-TGF-β1. However, the prodomain α1 and α5-helices orient differently on the GF domain (Fig. 1 *A*, *B*, *G*, and *H*). The BMP9 prodomain α5-helix inserts into the hydrophobic groove formed by the fingers of one GF monomer and the α3-helix of the other monomer (Fig. 1*A*). This association is stabilized by a cluster of specific interactions (Fig. 1*I*). Glu-248, at the N terminus of the α5-helix, forms salt bridges with GF residues Lys-393 and Lys-350. In the middle of the α5-helix, Met-252 plunges into a hydrophobic cavity. At the C terminus, His-255 stacks against GF residue Trp-322 (Fig. 1*I*). However, GF burial by the pro-BMP9 α5-helix (750 $Å^2$) is less than by the pro-TGF-β1 α1-helix (1,120 $Å^2$) or α1-helix plus latency lasso (1,490 $Å^2$). Furthermore, when crystals were cryo-protected with a 10% higher concentration of ethanol (3.25-Å dataset; Table S1), density for the α5-helix was present in one monomer but not the other (Fig. S6).

Prodomain Functions. We next asked if interactions of the two BMP9 prodomains with the GF dimer are independent or cooperative. Isothermal calorimetry (ITC) showed that, irrespective of whether increasing amounts of prodomain were added to GF or vice versa, heat production showed a single sigmoidal profile (Fig. 4 *A* and *B*). Curves fit well to a model in which the two binding sites are independent, and yielded K_D values of 0.8–1.0 μM at pH 4.5, which maintains BMP9 solubility.

A critical question concerning BMP prodomains is whether the BMP9 prodomain inhibits GF signaling and whether making the BMP9 prodomain dimeric as in pro-TGF-β1 would provide sufficient avidity to keep the GF latent. Consistent with previous

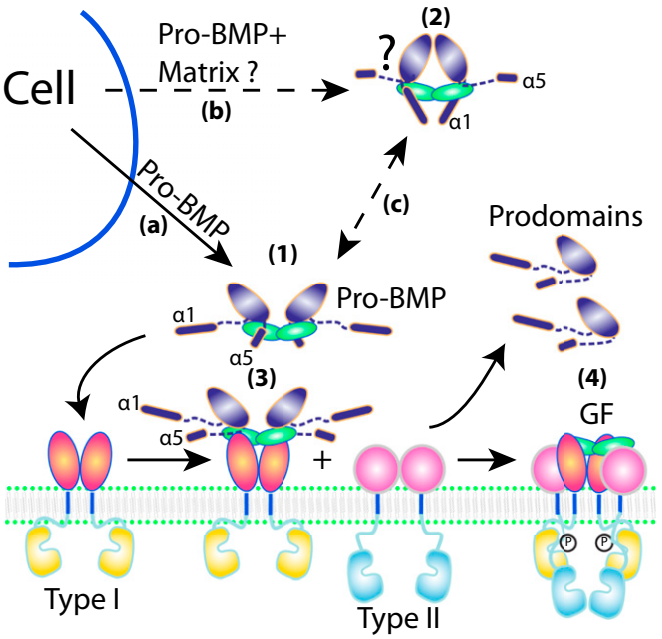

Fig. 5. Models for pro-BMP9 structures and binding to receptors. Models for the open-armed, nonlatent pro-BMP9 conformation characterized here (*1*), the proposed (dashed lines) pro-TGF-β1–like cross-armed conformation of pro-BMP9 (*2*), and stepwise binding (18) to type I (*3*) and type II receptors (*4*).

studies (16), pro-BMP9 and BMP9 showed little difference in inducing C2C12 cell differentiation, with EC_{50} values of 1.3 and 0.8 nM, respectively (Fig. 4*C*). However, by doing the experiment a different way, i.e., by titrating the prodomains into assays with 1 nM BMP9, we found that the prodomain is inhibitory, with IC_{50} = 79 nM (Fig. 4*D*). Thus, a large excess of the BMP9 prodomain over the GF is required to inhibit signaling, whereas at equimolar 1-nM concentrations of prodomain and GF monomers, the BMP9 prodomain has little effect on signaling. We added a cysteine-bearing GCN4 coil at the N terminus of the BMP9 prodomain to disulfide-link BMP9 prodomains into dimers or oligomers (Fig. S7). Multimerization modestly lowered the IC_{50} to 23 nM (Fig. 4*D*) but did not induce latency at equimolar concentrations.

To determine the basis for the partial inhibition of BMP9 signaling by the prodomain, we compared binding of receptor Fc fusions to pro-BMP9 and BMP9 in quantitative ELISA (Fig. 4 *E* and *F*). Among the seven type I receptors, ALK1 bound by far the strongest, and there was little difference in affinity and no difference in selectivity between BMP9 and pro-BMP9 (Fig. 4*E*). In contrast, the prodomain altered both EC_{50} values and selectivity of type II receptors (Fig. 4*F*). Whereas BMP9 bound ActRIIB and BMPRII similarly and 10-fold better than ActRIIA, pro-BMP9 bound ActRIIB 10-fold better than BMPRII and did not detectably bind ActRIIA (Fig. 4*F*). The EC_{50} values for type I and II receptors agree with previous affinity measurements with BMP9 (16, 17). Interestingly, the BMP7 prodomain also competes binding of BMP7 to type II but not type I receptors (18), consistent with the open-armed conformation of pro-BMP7 (Fig. 1*D*).

Discussion

BMPRII and ActRIIA are coexpressed with ALK1 and mediate BMP9 signaling in endothelial cells (12, 19). Furthermore, ALK1, which primarily functions as a receptor for BMP9 and BMP10, has recently been implicated as an important target of antiangiogenic tumor therapy (17). Together with the finding that BMP9 complexed with its prodomain circulates in the bloodstream at physiologically relevant concentrations (11), our finding that the BMP9 prodomain blocks binding to ActRIIA and alters selectivity for ActRIIB compared with BMPRII has important implications for BMP9 signaling in vivo.

The pro-BMP9 structure explains the selective effect of BMP prodomains on type II receptor binding (18) (Fig. 4*G*). The prodomain arm domain and α2-helix occupy the type II receptor binding site. In contrast, only the prodomain α5-helix blocks the type I receptor binding site (Fig. 4*G*). Selective displacement of the α5-helix by the type I receptor with retention of arm domain association is consistent with the relatively weak α5-helix interface described above. In contrast, arm domain binding to the type II receptor site is strong enough to alter receptor affinity and selectivity.

Antagonists including noggin, gremlins, and chordins bind to BMP GFs and regulate activity. However, little attention has been paid to whether BMP prodomains might prevent antagonist binding. Interestingly, the BMP-inhibiting fragment of the chordin family member crossveinless-2 binds to interfaces on BMP2 (20) similar to those on BMP9 to which the prodomain binds (Fig. 4*H*). The von Willebrand factor C (VWC) domain binds to a similar site on the GF fingers as the arm domain, whereas an N-terminal appendage called clip binds to the same site as the prodomain C-terminal appendage, the α5-helix (Fig. 4*H*). Whether prodomains can protect GF from inhibitors, as well as prevent GF binding to receptors, deserves study.

The crystal structure of pro-BMP9 begins to reveal how prodomains contribute to the tremendous functional diversity among the 33 members of the TGF-β family. Many of these members have prodomains that differ even more than BMP9 and TGF-β, which have only 11% sequence identity. Prodomain divergence may increase the specificity of GF signaling in vivo by regulating procomplex localization, movement, release, and activation in the extracellular environment.

The open-armed pro-BMP7 and 9 and cross-armed pro-TGF-β1 conformations differ greatly. Overall learnings from protein families that can adopt multiple conformations, such as tyrosine kinases, integrins, G protein-coupled receptors, membrane channels, and membrane transporters, show that when markedly distinct conformations are glimpsed for individual members, most family members can visit each state, often in a manner that is regulated by other interactors. Thus, we hypothesize that most members of the TGF-β family can visit both cross-armed and open-armed conformations. TGF-β is a later evolving family member; whereas BMPs and activins are found in all metazoans, TGF-β is found only in deuterostomes. Furthermore, TGF-β is the only known member with disulfide-linked arm domains. Thus, trapping pro-TGF-β in a solely cross-armed conformation with disulfides may be a later evolutionary adaptation.

The amino acid sequence of a protein is constrained by its structure, and sequence conservation in evolution is a powerful predictor of protein structure and conformation. The prodomain α1-helix has an important function in stabilizing the cross-armed conformation but has no function in the open-armed conformation, as shown by lack of electron density and presence of the prodomain α5-helix in a position that prevents α1-helix binding. In support of the hypothesis that pro-BMP9 can adopt a cross-armed conformation, the amino acid sequence corresponding to the α1-helix is highly conserved (44–79% identity at residues 29–47) among human, mouse, zebrafish, and chicken BMP9s. Indeed, the sequence of the α1-helix is more conserved than the remainder of the prodomain (33–74% identity). Furthermore, the prodomain α1-helix sequence and its amphipathic signature are also conserved among diverse representatives of the 33-member TGF-β family including BMP7 (Fig. 2*B*). Importantly, the α1-helix and its amphipathic signature are highly conserved between pro-TGF-β1 and pro-BMP9 (Fig. 2). These results support the hypothesis that pro-BMP9 and other TGF-β family members can adopt an α1-helix-bound, cross-armed conformation similar to that of TGF-β1.

To more directly test evolutionary support for a cross-armed BMP9 conformation, we made a pro-TGF-β1–like model of pro-BMP9 that uses the BMP9 conformation of the arm domains, superimposed on the cross-armed orientation of the arm domains in pro-TGF-β1, and pro-TGF-β1–like conformations of prodomain α1- and α2-helices and GF domains (Movie S1). In addition to the α1-helix, pro-BMP9 also includes a latency lasso-like sequence, including an identical PSQ sequence (Fig. 2*A*). There are no clashes between the two pro-BMP9 arm domains in the crossed-arm conformation; notably, the arm domains come close together at their β4 and β5-strands, which are on the side of the arm domain conserved between pro-BMP9 and pro-TGF-β1 (Movie S1). The extensive, amphipathic α1-helix–GF interface in pro-TGF-β1 is recapitulated well in the cross-armed pro-BMP9 model, and the long α5-helix can adopt a conformation similar to the shorter α5-helix in pro-TGF-β1 without clashes (Fig. 1*K*). These results compellingly support a cross-armed conformation for pro-BMP9. A plausible pathway for structural interconversion between open-armed and cross-armed conformations of BMP9 can be described in which crossing of the arms is accompanied by dissociation of the α5-helix from the GF and its replacement by the α1-helix and latency lasso (Movie S1).

The strong evolutionary and 3D structural support for a cross-armed conformation of BMP9 (and also BMP7; Fig. 2*B*) contrasts with our lack of observation of cross-armed BMP7 and BMP9 conformations in EM (Fig. 1 *C* and *D*). However, this is easily explicable, because it is compatible with a lower energy of the open-armed conformation for the isolated procomplex, and on the other hand, with a lower energy of the cross-armed conformation for the procomplex bound to an interactor. For BMPs in bone, such interactors may be present in the residual matrix, and release from interactors may in part be responsible for the increase in BMP activity found after extraction by denaturants and purification (2).

We hypothesize that cross-armed and open-armed conformations of TGF-β family members correspond to latent and nonlatent states, respectively, and propose a model for conformational regulation of release from storage and latency (Fig. 5). Some family members may be secreted as isolated procomplexes in signaling-competent, open-armed conformations (Fig. 5, pathway a and structure 1). Other family members may be secreted together with or immediately form complexes after secretion with extracellular matrix components including heparin, proteoglycans, fibrillin, and latent TGF-β binding proteins (8, 9, 21–23). These interactors may stabilize the cross-armed conformation (Fig. 5, pathway b and structure 2), and enable the GF domain, which is very short lived in vivo, to remain latent and reach storage concentrations as high as 100 ng/g in demineralized bone (24). Release from storage in vivo may then yield the open-armed conformation, which is ready for receptor or inhibitor binding (Fig. 5, pathway c).

TGF-β family members with long sequences at the ends of their prodomains that may have α5-helix–like functions include BMP3, BMP10, BMP15, GDF5, 6, 7, and 9, anti-Müllerian hormone, and nodal (Fig. S5). A number of these, including BMP9 and BMP10, have basic sequences resembling PC cleavage sites (25) in or before the α5-helix (Fig. 2*A* and Fig. S5). Moreover, many TGF-β family members have PC or tolloid cleavage sites in or after the prodomain α1-helix that regulate activation or signaling (6, 7, 9, 10, 25) (Fig. S5). Indeed, recombinant pro-BMP9 preparations contain a minor component cleaved at a putative PC site in this region (Fig. 2*A* and *Methods*). Thus, potential mechanisms for regulating the switching between open-armed and cross-armed procomplex conformations include removal of the α1- or α5-helix by proteases in addition to binding to extracellular matrix components. Our results suggest that the open-armed conformation of pro-BMP9 can readily bind to type I receptors, with displacement of the α5-helix (Fig. 5, structure 3). The final step in signaling could then be binding to type II receptors, with complete prodomain dissociation, consistent with a previous model of stepwise receptor binding and prodomain displacement (18) (Fig. 5, structure 4).

Methods

Pro-BMP9 and pro-BMP7 were purified from supernatants of CHO and HEK293 cell transfectants, respectively. Crystals formed in 0.15 M zinc acetate, 0.1 M sodium cacodylate, pH 5.8, and 4% (vol/vol) isopropanol. Phases were solved using Zn anomalous diffraction. Complete methods are described in *SI Methods*.

1. Wang EA, et al. (1988) Purification and characterization of other distinct bone-inducing factors. *Proc Natl Acad Sci USA* 85(24):9484–9488.
2. Luyten FP, et al. (1989) Purification and partial amino acid sequence of osteogenin, a protein initiating bone differentiation. *J Biol Chem* 264(23):13377–13380.
3. Celeste AJ, et al. (1990) Identification of transforming growth factor beta family members present in bone-inductive protein purified from bovine bone. *Proc Natl Acad Sci USA* 87(24):9843–9847.
4. Cui Y, et al. (2001) The activity and signaling range of mature BMP-4 is regulated by sequential cleavage at two sites within the prodomain of the precursor. *Genes Dev* 15(21):2797–2802.
5. Harrison CA, Al-Musawi SL, Walton KL (2011) Prodomains regulate the synthesis, extracellular localisation and activity of TGF-β superfamily ligands. *Growth Factors* 29(5):174–186.
6. Constam DB (2014) Regulation of TGFβ and related signals by precursor processing. *Semin Cell Dev Biol* 32:85–97.
7. Akiyama T, Marqués G, Wharton KA (2012) A large bioactive BMP ligand with distinct signaling properties is produced by alternative proconvertase processing. *Sci Signal* 5(218):ra28.
8. Gregory KE, et al. (2005) The prodomain of BMP-7 targets the BMP-7 complex to the extracellular matrix. *J Biol Chem* 280(30):27970–27980.
9. Sengle G, Ono RN, Sasaki T, Sakai LY (2011) Prodomains of transforming growth factor β (TGFβ) superfamily members specify different functions: Extracellular matrix interactions and growth factor bioavailability. *J Biol Chem* 286(7):5087–5099.
10. Shi M, et al. (2011) Latent TGF-β structure and activation. *Nature* 474(7351):343–349.
11. Bidart M, et al. (2012) BMP9 is produced by hepatocytes and circulates mainly in an active mature form complexed to its prodomain. *Cell Mol Life Sci* 69(2):313–324.
12. Chen H, et al. (2013) Context-dependent signaling defines roles of BMP9 and BMP10 in embryonic and postnatal development. *Proc Natl Acad Sci USA* 110(29):11887–11892.
13. Castonguay R, et al. (2011) Soluble endoglin specifically binds bone morphogenetic proteins 9 and 10 via its orphan domain, inhibits blood vessel formation, and suppresses tumor growth. *J Biol Chem* 286(34):30034–30046.
14. David L, Feige JJ, Bailly S (2009) Emerging role of bone morphogenetic proteins in angiogenesis. *Cytokine Growth Factor Rev* 20(3):203–212.
15. Wooderchak-Donahue WL, et al. (2013) BMP9 mutations cause a vascular-anomaly syndrome with phenotypic overlap with hereditary hemorrhagic telangiectasia. *Am J Hum Genet* 93(3):530–537.
16. Brown MA, et al. (2005) Crystal structure of BMP-9 and functional interactions with pro-region and receptors. *J Biol Chem* 280(26):25111–25118.
17. Townson SA, et al. (2012) Specificity and structure of a high affinity activin receptor-like kinase 1 (ALK1) signaling complex. *J Biol Chem* 287(33):27313–27325.
18. Sengle G, Ono RN, Lyons KM, Bächinger HP, Sakai LY (2008) A new model for growth factor activation: Type II receptors compete with the prodomain for BMP-7. *J Mol Biol* 381(4):1025–1039.
19. Scharpfenecker M, et al. (2007) BMP-9 signals via ALK1 and inhibits bFGF-induced endothelial cell proliferation and VEGF-stimulated angiogenesis. *J Cell Sci* 120(Pt 6): 964–972.
20. Zhang JL, et al. (2008) Crystal structure analysis reveals how the Chordin family member crossveinless 2 blocks BMP-2 receptor binding. *Dev Cell* 14(5):739–750.
21. Sengle G, et al. (2008) Targeting of bone morphogenetic protein growth factor complexes to fibrillin. *J Biol Chem* 283(20):13874–13888.
22. Li S, et al. (2010) Activin A binds to perlecan through its pro-region that has heparin/heparan sulfate binding activity. *J Biol Chem* 285(47):36645–36655.
23. Anderson SB, Goldberg AL, Whitman M (2008) Identification of a novel pool of extracellular pro-myostatin in skeletal muscle. *J Biol Chem* 283(11):7027–7035.
24. Pietrzak WS, Woodell-May J, McDonald N (2006) Assay of bone morphogenetic protein-2, -4, and -7 in human demineralized bone matrix. *J Craniofac Surg* 17(1): 84–90.
25. Seidah NG, Prat A (2012) The biology and therapeutic targeting of the proprotein convertases. *Nat Rev Drug Discov* 11(5):367–383.
26. Krissinel E, Henrick K (2004) Secondary-structure matching (SSM), a new tool for fast protein structure alignment in three dimensions. *Acta Crystallogr D Biol Crystallogr* 60(Pt 12 Pt 1):2256–2268.

Supporting Information

Mi et al. 10.1073/pnas.1501303112

SI Methods

Expression and Purification of Mouse–Human Chimeric BMP9. CHO cells stably expressed full-length pro-BMP9 containing the mouse prodomain and human GF domain. Cells were seeded in roller bottles in a 50:50 (vol/vol) mix of F12 and DMEM supplemented with nonessential amino acids, biotin, vitamin B_{12}, 0.2 μM methotrexate, and 10% (vol/vol) FBS and grown for 3–4 d to near confluence. Serum-containing growth medium was discarded, roller bottles were rinsed with PBS, and a serum-free production medium was added containing nonessential amino acids, 5 μg/mL insulin, 12.9 μM putrescine, 0.2 μM hydrocortisone, 29 nM selenium, and 0.6 g/L polyvinyl alcohol. Conditioned medium (CM) was collected at 48 h, and roller bottles were refed with fresh serum-free medium. Two sequential 48-h harvests were collected. CM was clarified by passing through a 5-μm pore filter (pass Profile) and a 0.22-μm pore Duropore filter (Millipore) (Patent: BMP9 Compositions WO 1995033830 A).

In a typical purification, the BMP9 procomplex was captured from ∼20 L of CHO CM by loading onto a 265-mL, 5.0 × 13.5-cm Q-Sepharose column equilibrated with 20 mM Tris, pH 8.6 (buffer A). After washing with 10 column volumes (CVs) of buffer A, BMP9 procomplex was eluted in a single step with buffer A containing 1.0 M NaCl.

To purify pro-BMP9, the main peak was exchanged into buffer A plus 30 mM NaCl with a 735-mL, 5.0 × 37.4-cm Sephadex G25 size-exclusion chromatography (SEC) column. The peak (720 mg total protein) was divided into thirds and loaded onto an 8-mL, 1.0 × 10.2-cm Source 15Q column equilibrated with 50 mM Mes, pH 6.1. After a 10-CV wash with equilibration buffer, the BMP9 procomplex was eluted with a 12-CV gradient of 0.03–1 M NaCl in 50 mM Mes, pH 6.1. SDS/PAGE and analytical SEC showed that pro-BMP9 eluted between 0.15 and 0.32 M NaCl. Pooled fractions from the Source15Q step (240 mg total protein from three runs) were further purified with three SECs on two tandem 2.15 × 60-cm TOSOH G3000SWL columns equilibrated with PBS (total CV = 435 mL). Pro-BMP9 and free BMP9 prodomain eluted in separate peaks as shown by SDS/PAGE and analytical SEC and were pooled separately, sterilized with a 0.22-μm syringe filter, and stored at 4 °C. Final yield was 125 mg (6.25 mg/L CM). Material was characterized by SDS/PAGE and N-terminal sequencing of individual Coomassie blue-stained bands. Present in the preparation was a putatively uncleaved prodomain GF precursor that yielded the N-terminal prodomain sequence, the prodomain that yielded a major sequence beginning with the N-terminal sequence and a minor sequence beginning at prodomain residue 46 (SLN), and a GF that yielded the GF sequence of SAG beginning at residue 298.

To purify mature BMP9, the main peak from the Q-Sepharose step of a separate purification run (720 mg total protein) was diluted with 19 volumes of 6 M urea, 25 mM Mes, and 25 mM Hepes, pH 6.5 and loaded onto a 265-mL, 5.0 × 13.5-cm Q-Sepharose column in tandem with a 15 mL, 1.6 × 7.5-cm SP-Sepharose column, both equilibrated with the same buffer. After washing with equilibration buffer, the columns were separated, and BMP9 was eluted from the SP-Sepharose column with a 12 CV gradient of 0–1 M NaCl in 6 M urea, 25 mM Mes, and 25 mM Hepes, pH 6.5. BMP9 eluted between 0.25 and 0.4 M NaCl. Fractions containing mature BMP9 were identified by SDS/PAGE and pooled. Protein (13.3 mg total) was further purified with two SECs on two tandem 2.15 × 60-cm TOSOH G3000SWL columns equilibrated with 6 M urea, 0.3 M NaCl, 25 mM Mes, and 25 mM Hepes, pH 6.5. Fractions containing mature BMP9 were identified by SDS/PAGE and pooled. Purified protein (11.4 mg) was concentrated on Amicon-ultra-15 centrifugal concentration devices and dialyzed into 5 mM NaCl, 10% (vol/vol) glycerol, 2.5% (wt/vol) glycine, and 5 mM glutamic acid, pH 4.5 centrifuged at 1,400 × *g*, sterilized with a 0.22-μm syringe filter, supplemented with 0.01% Tween-80, and stored at 4 °C. The final yield was 9.1 mg (0.46 mg/L CM).

For purification of the prodomain, pro-BMP9 in PBS was mixed with an equal volume of a 9:1 (vol/vol) solution of ethanol:1 M sodium acetate, pH 4.4. The mixture was incubated on ice for 1 h. Precipitated BMP9 prodomain was collected by centrifugation at 20,000 × *g* for 10 min and dissolved in 20 mM Tris, pH 8.0. BMP9 prodomain was further purified by ion exchange chromatography in the same buffer with a gradient of 0–1 M NaCl and S200 SEC.

Crystallization, Data Collection, and Structure Determination. For crystallization, pro-BMP9 in PBS was further purified by Superdex 200 HR SEC in 20 mM Bis-Tris-propane, pH 8.0, and 50 mM NaCl, and concentrated to 6 mg/mL. Screening using sparse-matrix, hanging drop vapor diffusion yielded a hit in 0.2 M zinc acetate, 0.1 M Mes, pH 6.0, and 15% (vol/vol) ethanol. Fine-matrix and additive screening found a final crystallization condition of 0.15 M zinc acetate, 0.1 M sodium cacodylate, pH 5.8, 4% (vol/vol) isopropanol, and 0.15 M nondetergent sulfobetaine (NDSB-211). Crystals were cryo-protected by rapid transfer to either 30% (vol/vol) ethanol (3.25-Å dataset) or 20% ethanol/10% glycerol (vol/vol) (3.3-Å dataset) in mother liquor and flash-frozen in liquid nitrogen.

X-ray diffraction data were collected at the Northeastern Collaborative Access Team beamline of Advanced Photon Source, Argonne, IL, and processed with X-ray Detector Software (1). For refinement of the 3.3-Å structure, eight datasets collected from eight isomorphic crystals were merged together. Initial phases were determined, and models were built using molecular replacement with single wavelength anomalous scattering, (2) using the BMP9 dimer (3) as a search model and weak zinc anomalous diffraction at 0.97918 Å in our 3.3-Å dataset. Subsequently, more accurate phases were solved using SAD in Phenix (2) with anomalous data collected at a zinc absorption peak at 1.2823 Å in a thin-sliced (0.2° oscillation per frame over 360° oscillation range), low-dose (1% transmission) mode using a PILATUS 6M detector. A total of 11 zinc binding sites were found by the program, and the electron density was well resolved, giving a figure of merit of 0.75. As the data for phasing and refinement are not isomorphic (Table S1), phases were transferred to the 3.3-Å dataset using density_cut in Phenix (2) and Molrep in CCP4 (4). Phases were extended to higher-resolution shells by solvent flattening and multicrystal averaging using the 3.3- and 3.6-Å datasets in Phenix (2). The 3.25-Å dataset was solved by molecular replacement using the structure from the 3.3-Å dataset.

Model building with Coot (5) and refinement with Phenix including phenix.rosetta_refine (2) were iterated many times. The resolution of the data was determined using paired refinement (6). In each asymmetric unit, there are two pro-BMP9 protomers, which form a functional dimer.

Superimposition. Arm domain superimposition was with pro-BMP9 residues 84–92, 107–115, 116–132, 143–155, 164–175, 177–197, and 226–237; pro-TGF-β1 residues 77–85, 101–109, 115–131, 135–147, 148–159, 164–184, and 224–235; and "super" in PyMol.

ELISA. BMP9 or pro-BMP9 was coated overnight at 4°C in PBS at 1 μg/mL on Nunc MediSorb 96-well plates. Plates were washed with PBST (PBS with the addition of 0.05% Tween 20) and blocked with 2% (wt/vol) BSA in PBST for 5–8 h at 20 °C. Blocking solutions were decanted, and receptor-Fc fusion proteins (R&D Systems, except ActRIIB-Fc, which was made in-house) were applied at 2 μg/mL and 1:3 serial dilutions in PBST with 2% (wt/vol) BSA and incubated at 4 °C overnight. Plates were washed three times with PBST, followed by the addition of JDC-10 mouse anti-human Fc conjugated with HRP (Southern Biotech) at 1:5,000 in PBST + 1% BSA. After overnight incubation at 4 °C, plates were washed with PBST (0.05% Tween 20), and color was developed with a standard 3,3′,5,5′ tetramethylbenzidine reagent. After stopping with 1 M H_2SO_4, plates were read at 450 nm. Binding data were plotted as the percentage of maximal receptor Fc bound in each experiment and fit to an equation for fractional saturation. Reported EC_{50} values represent the average and SD from triplicate experiments.

Pro-BMP7 Expression and Purification. HEK293 cells that stably express WT pro-BMP7 were kindly provided by Lynn Sakai, Shriners Hospital for Children, Portland, OR (7). Cells were cultured in DMEM with 10% (vol/vol) FBS and 0.5 mg/mL G418. Supernatants (2 L) were clarified by centrifugation, concentrated 10-fold with tangential flow filtration (Vivaflow 200; Sartorius Stedim), diluted 5-fold with Tris-buffered saline, pH 8.0 (TBS), and then concentrated 5-fold. The material was loaded onto 20 mL Ni-NTA agarose (Qiagen), washed with 200 mL of 1 M NaCl, 25 mM imidazole, and 20 mM Tris·HCl, pH 8.0, and eluted by 0.5 M NaCl and 1 M imidazole, pH 8.0. The Ni-NTA eluent containing pro-BMP7 was purified by SEC using a HiLoad 26/60 Superdex-200 prep grade column (GE Healthcare) in TBS. The pro-BMP7–containing fractions were pooled and further purified with a heparin Hitrap column (GE Healthcare), followed by Superdex S200 SEC in TBS. The peak fractions containing pure pro-BMP7 were pooled and concentrated using a 50-kDa cutoff centrifugal concentrator (Vivaspin) to 20 mg/mL, frozen in liquid nitrogen, and stored at −80 °C.

BMP9 Prodomain with a Coiled-Coil. A signal sequence, Strep-tag, His-tag, 3C protease cleavage site, and GCN4 coiled-coil were fused to the N terminus of the human BMP9 prodomain. The C-terminal Val-30 residue of GCN4 [numbering of Harbury et al. (8)] was mutated to cysteine. The construct in pEF1-puro was transiently transfected into HEK 293T cells (9). After culture for 3 d in Freestyle 293 medium, medium was concentrated, and buffer was exchanged with 20 mM Tris, pH 8.0, and 200 mM NaCl. Protein was purified by Strep-tactin affinity chromatography.

C2C12 Differentiation Assay. The C2C12 cell line was from American Type Culture Collection. p-Nitrophenyl phosphate was from Sigma-Aldrich. Activity of BMP9 was measured as previously described (10, 11) using induction of alkaline phosphatase, a biomarker of osteogenesis, in myoblast C2C12 cells. C2C12 cells seeded at 10^4 cells per well in 96-well plates 1 d previously in DMEM/10% (vol/vol) FBS were washed two times and suspended in 100 μL DMEM. Test proteins in 100 μL DMEM and 1 mg/mL BSA were added in triplicate. After 2 d, wells were washed with PBS, 50 μL distilled water was added, and plates were frozen and thawed three times. Freshly made 0.1 M glycine, pH 10.3, 0.1% Triton X-100, 19 mM p-nitrophenyl phosphate, and 17 mM $MgCl_2$ (50 μL) was added. After 30 min at 37 °C, 100 μL 0.2 N NaOH was added, and alkaline phosphatase activity was measured at 405 nm.

ITC. Proteins were dialyzed overnight against 0.5% sucrose, 5 mM NaCl, 0.01% Tween 80, 2.5% (wt/vol) glycine, and 5 mM glutamic acid, pH 4.5, degassed, and centrifuged at 20,000 × *g* for 10 min. ITC experiments used MicroCal iTC200 (GE Healthcare Life Sciences). Either 94.8 μM BMP9 prodomain was titrated into 5 μM BMP9 dimer in the cell or 47.4 μM BMP9 dimer was titrated into 10 μM BMP9 prodomain in the cell. A priming injection of 0.4 μL (not included in data analysis) was followed by 2-μL injections every 300 s. Data averaged over 2-s windows were analyzed using Origin 7. Fits using cooperative binding or two sequential binding sites did not yield markedly lower χ^2 values than a single-binding-site model, which was used to fit N (binding sites), K_a (association constant), and ΔH (enthalpy).

Negative-Stain EM. Pro-BMP9 and pro-BMP7 were purified by SEC using Superdex 200 HR preequilibrated with 20 mM Tris, pH 8.0, and 150 mM NaCl. The peak fraction was loaded onto glow-discharged carbon-coated grids, buffer was wicked off, and grids were immediately stained with 0.75% (wt/vol) uranyl formate. EM was as previously described (12). Images were recorded with a CCD camera at 52,000× magnification with a defocus of −1.5 μm. The pixel size was 2.88 Å at specimen level. Particles were interactively picked with BOXER in EMAN (13). Class averages were calculated with SPIDER (14) as previously described (12).

1. Kabsch WF (2001) Crystallography of biological macromolecules. *International Tables for Crystallography*, eds Rossmann MG, Arnold E (Kluwer Academic Publishers, Dordrecht), pp 730–734.
2. Adams PD, et al. (2010) PHENIX: a comprehensive Python-based system for macromolecular structure solution. *Acta Crystallogr D Biol Crystallogr* 66(Pt 2):213–221.
3. Brown MA, et al. (2005) Crystal structure of BMP-9 and functional interactions with pro-region and receptors. *J Biol Chem* 280(26):25111–25118.
4. Bailey S; Collaborative Computational Project, Number 4 (1994) The CCP4 suite: Programs for protein crystallography. *Acta Crystallogr D Biol Crystallogr* 50(Pt 5): 760–763.
5. Emsley P, Cowtan K (2004) Coot: model-building tools for molecular graphics. *Acta Crystallogr D Biol Crystallogr* 60(Pt 12 Pt 1):2126–2132.
6. Karplus PA, Diederichs K (2012) Linking crystallographic model and data quality. *Science* 336(6084):1030–1033.
7. Gregory KE, et al. (2005) The prodomain of BMP-7 targets the BMP-7 complex to the extracellular matrix. *J Biol Chem* 280(30):27970–27980.
8. Harbury PB, Zhang T, Kim PS, Alber T (1993) A switch between two-, three-, and four-stranded coiled coils in GCN4 leucine zipper mutants. *Science* 262(5138):1401–1407.
9. Mi LZ, et al. (2008) Functional and structural stability of the epidermal growth factor receptor in detergent micelles and phospholipid nanodiscs. *Biochemistry* 47(39): 10314–10323.
10. Partridge NC, et al. (1981) Functional properties of hormonally responsive cultured normal and malignant rat osteoblastic cells. *Endocrinology* 108(1):213–219.
11. Rosen V, et al. (1994) Responsiveness of clonal limb bud cell lines to bone morphogenetic protein 2 reveals a sequential relationship between cartilage and bone cell phenotypes. *J Bone Miner Res* 9(11):1759–1768.
12. Mi LZ, et al. (2011) Simultaneous visualization of the extracellular and cytoplasmic domains of the epidermal growth factor receptor. *Nat Struct Mol Biol* 18(9):984–989.
13. Ludtke SJ, Baldwin PR, Chiu W (1999) EMAN: semiautomated software for high-resolution single-particle reconstructions. *J Struct Biol* 128(1):82–97.
14. Frank J, et al. (1996) SPIDER and WEB: processing and visualization of images in 3D electron microscopy and related fields. *J Struct Biol* 116(1):190–199.

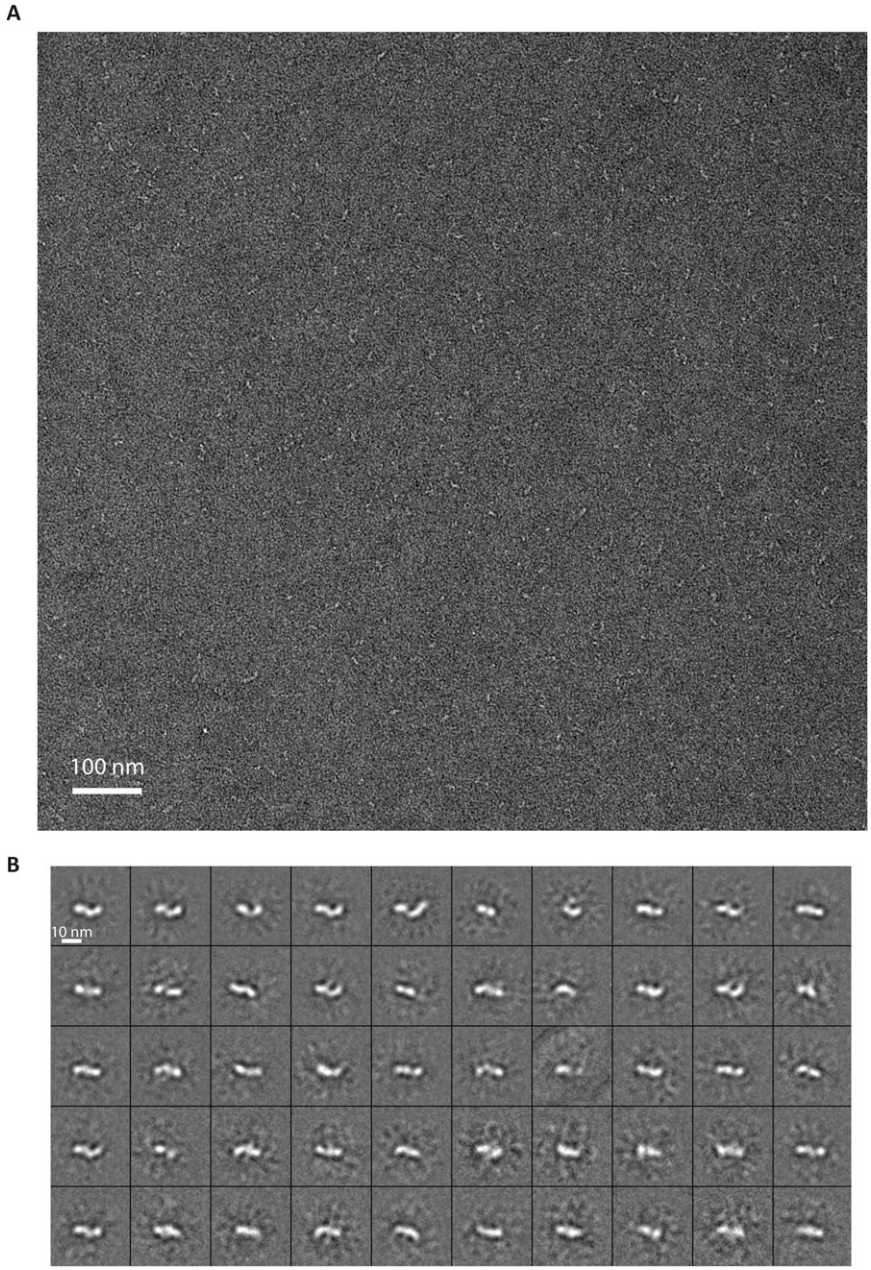

Fig. S1. Pro-BMP9 EM structure. Representative electron micrograph (*A*) and all 50 class averages of 7,098 particles (*B*). Averages are ranked (left to right in each row, from top to bottom row) by numbers of particles in each class.

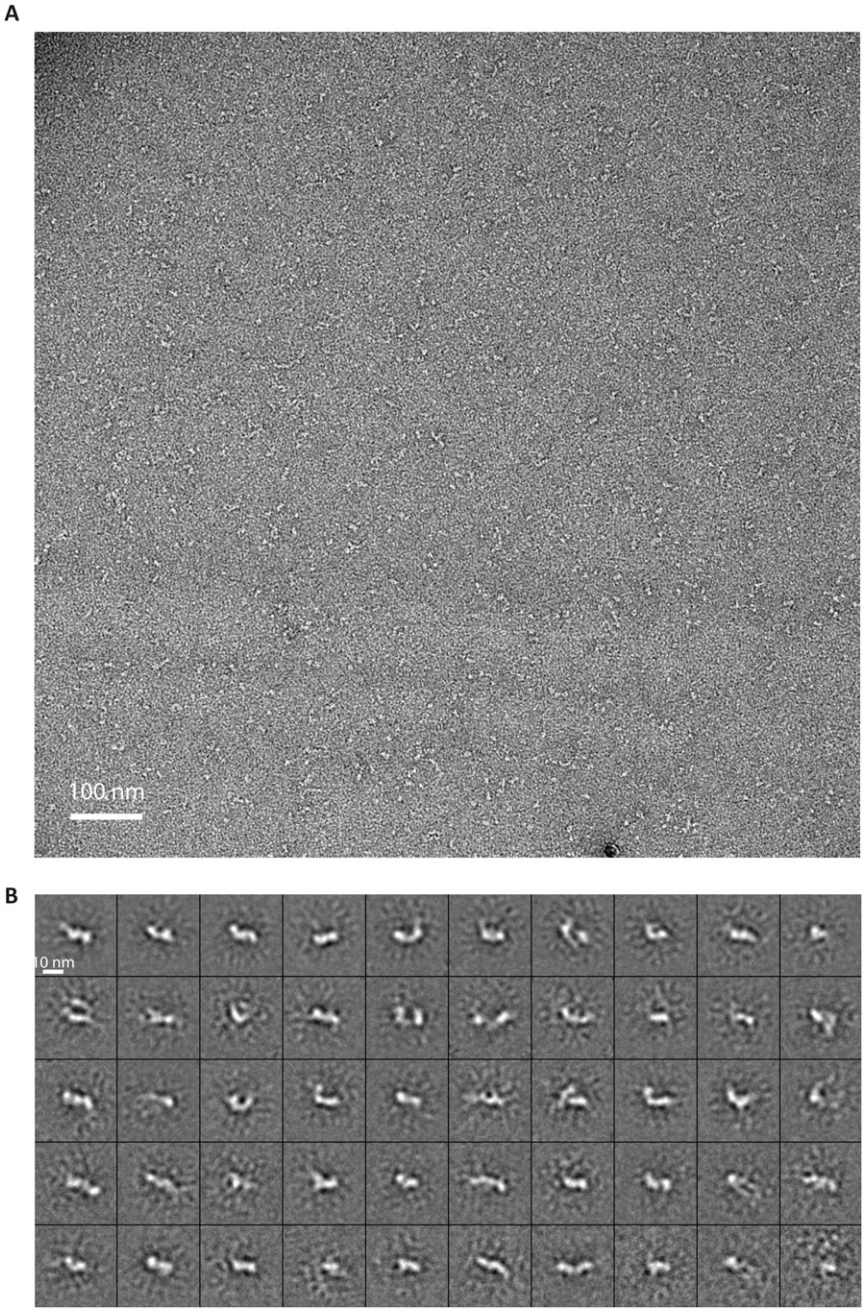

Fig. S2. Pro-BMP7 EM structure. Representative electron micrograph (*A*) and all 50 class averages of 4,427 particles (*B*). Averages are ranked (left to right in each row, from top to bottom row) by numbers of particles in each class.

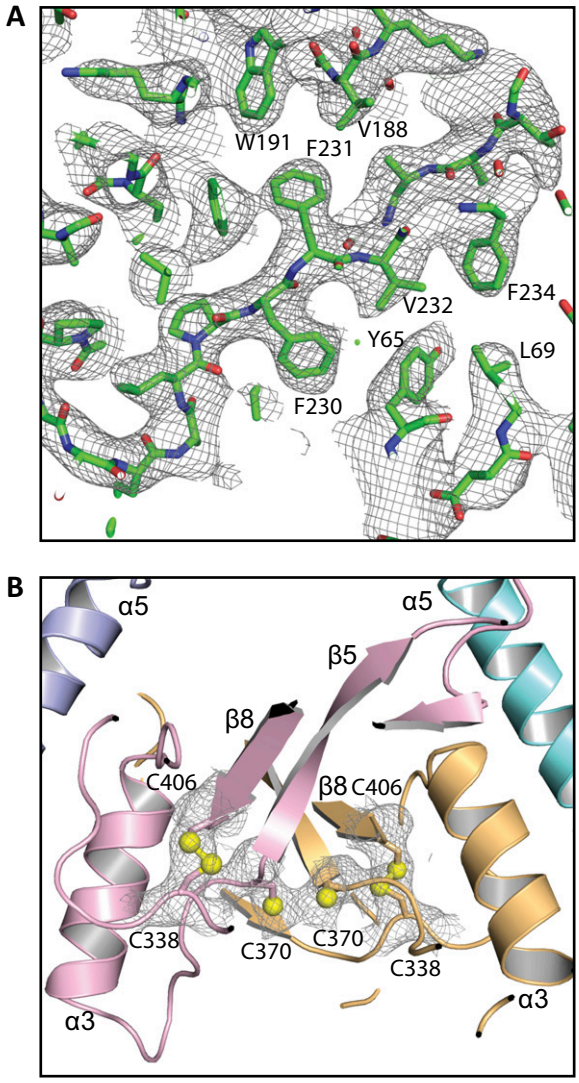

Fig. S3. Electron density map of pro-BMP9. (*A*) Representative region of experimentally phased electron density map of pro-BMP9 shown with mesh at 1σ contour level. (*B*) The free cysteines at the dimer interface and nearby disulfides shown with stick and S atom spheres, with experimentally phased electron density at 1σ level carved within 3 Å of cysteine residues. The structure appears to contain a mixture of disulfide and nondisulfide bonded Cys-370 residues at the GF monomer-monomer interface, consistent with presence of both GF monomers and dimers in nonreducing SDS/PAGE (Fig. S7 right, lane 2). In the refined molecular model, the disulfide is not built.

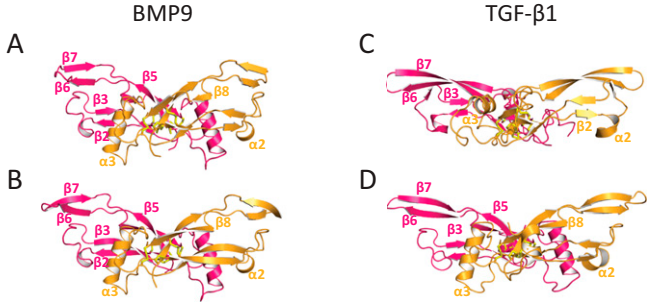

Fig. S4. Comparison of BMP9 and TGF-β1 structures in different complexes. (*A* and *B*) Comparison of prodomain-associated BMP9 (*A*) with receptor-bound BMP9 [Protein Data Bank (PDB) ID 4FAO] (*B*). (*C* and *D*) Comparison of prodomain-associated TGF-β1 (PDB ID 3RJR) (*C*) with receptor-bound TGF-β1 (PDB ID 3KFD) (*D*). The structures are represented in cartoon with one growth factor in pink and the other in gold.

Fig. S5. Alignment of human TGF-β family sequences including structurally aligned pro-TGF-β1 and pro-BMP9 sequences. Black dots mark decadal residues. Gold dots mark residues with >50% surface accessible surface area buried in prodomain-GF interfaces. Potential proprotein convertase cleavage sites and tolloid cleavage sites are marked with green and red circles, respectively. BMP8 shows BMP8A sequence which is almost identical to BMP8B.

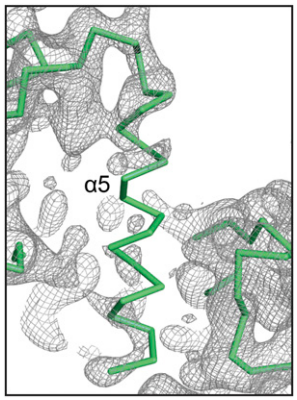

Fig. S6. Poor α5-helix density in one monomer of pro-BMP9 in the 3.25 Å dataset. Simulated annealing composite omit map is shown in mesh contoured at 1σ. The crystal was cryo-protected with 30% ethanol plus mother liquor.

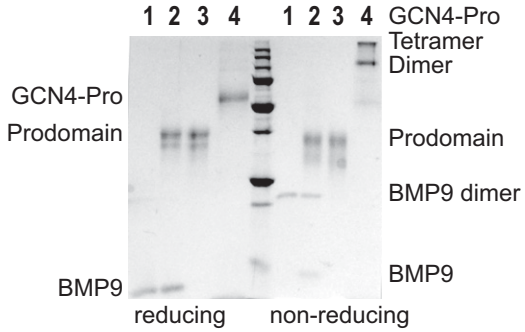

Fig. S7. Coomassie-stained SDS/PAGE of proteins used in crystallization and functional studies. Purified samples were loaded at equal molar amount: 1, BMP9; 2, pro-BMP9; 3, BMP9 prodomain; 4, GCN4-prodomain.

Table S1. Data collection and refinement statistics

	Zinc anomalous peak	Cryo with 20% ethanol/10% glycerol	Cryo with 30% ethanol
Wavelength (Å)	1.2823	0.97918	1.0332
Resolution range (Å)*	50.0–3.6 (3.69–3.60)	50.0–3.3 (3.39–3.30)	50.0–3.25 (3.33–3.25)
Space group	P 32 2 1	P 32 2 1	P 32 2 1
Unit cell a, b, c (Å)	121.9, 121.9, 223.6	120.8, 120.8, 220.6	120.3, 120.3, 221.3
α, β, γ (°)	90, 90, 120	90, 90, 120	90, 90, 120
Unique reflections*,†	31,412 (3,191)	29,933 (2,973)	29,711 (2,147)
Multiplicity*	14.5 (13.5)	23.3 (23.9)	4.03 (4.10)
Completeness (%)*	99.9 (99.9)	99.6 (100.0)	99.5 (99.7)
I/ σ(I)*	10.08 (0.43)	9.97 (0.67)	8.36 (0.53)
Wilson B-factor	136.5	142.7	128.2
R_{merge}*,‡	0.190 (4.82)	0.277 (5.26)	0.133 (3.394)
CC1/2 (%)*,§	0.999 (0.139)	0.994 (0.161)	0.995 (0.123)
Phasing and refinement			
Phasing FOM¶		0.75(0.29)	
Resolution range (Å)*		50.0–3.3 (3.36–3.30)	50.0–3.25 (3.35–3.25)
R_{work}/R_{free}*,‖		0.213/0.230 (0.335/0.314)	0.240/0.260 (0.387/0.384)
Nonhydrogen atoms			
Protein/NAG/Zn/water		4,802/56/10/21	4,681/42/10/14
RMSD bonds (Å)		0.002	0.002
RMSD angles (°)		0.59	0.62
Ramachandran plot**		93/7/0	93/7/0
(% favored/allowed/outliers)			
Clashscore**		3.03	5.06
Average B-factor		172.4	147.7
Macromolecules		171.8	147.2
Solvent		130.9	104.3
Protein databank codes		4YCG	4YCI

*Statistics for the highest-resolution shell are shown in parentheses.

†Friedel pairs are treated as separate reflections.

‡$R_{merge} = \sum_{hkl}\sum_{j}|\mathbf{I}_{hkl} - \mathbf{I}_{hkl}(J)|/\sum_{hkl}\sum_{j}|\mathbf{I}_{hkl}(J)|$, where $\mathbf{I}_{hkl}(J)$ and $\mathbf{I}_{hkl}$ are the jth and mean measurement of the intensity of reflection hkl.

§Pearson's correlation coefficient between average intensities of random half-data sets of the measurements for each unique reflection.

¶The value in parentheses is the figure of merit determined without solvent flattening and noncrystallographic symmetry averaging.

‖$R_{work} = \sum_{hkl}||\mathbf{F}_{obs}| - |\mathbf{F}_{calc}||/|\mathbf{F}_{obs}|$, where $\mathbf{F}_{obs}$ and $\mathbf{F}_{calc}$ are the observed and calculated structure factors, respectively. R_{free} is the cross-validation R factor computed for the 5% test set of unique reflections.

**Ramachandran and clash values were reported by Phenix.

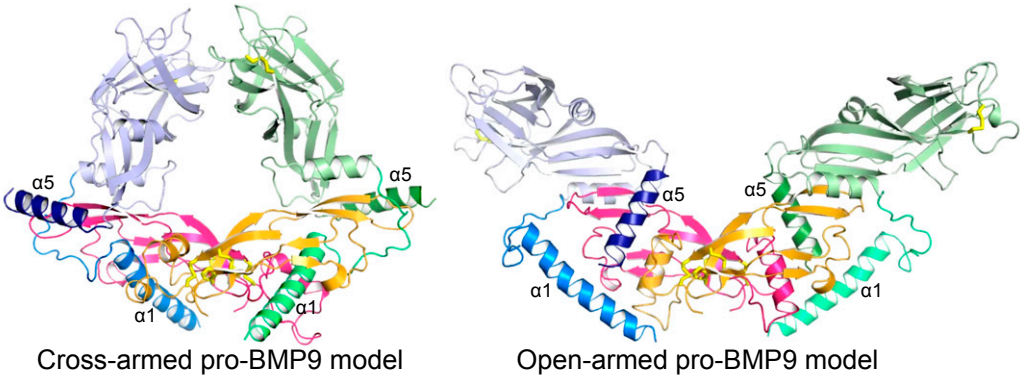

Movie S1. A feasible pathway for conformational change of pro-BMP9 between open-armed and cross-armed conformations. A cross-armed model of pro-BMP9 was constructed as described in *Discussion*. The movie, if looped, will display reversible conformational change from cross-armed to open-armed and open-armed to cross-armed. Structures are shown in cartoon with yellow disulfide bonds. BMP9 is shown with magenta and orange monomers. Prodomain monomers are shown in blue and green. Different shades are used for different elements. Thus for the prodomain monomer on the left, the arm domain and α2-helix are light blue, the α1-helix plus latency loop are marine, and the α5-helix is dark blue. The cross-armed pro-BMP9 model accommodates the longer α5-helix of pro-BMP9 in the same position as the shorter α5-helix of pro-TGF-β1. The open-armed pro-BMP9 model adds the α1-helix and the straight jacket elements to the pro-BMP9 crystal structure in positions where they do not clash. Using the open-armed and cross-armed models as starting and ending states, 88 morphing states in-between were calculated with adiabatic mapping using the script morph_dist from the Morph Server (1).

Movie S1

1. Krebs WG, Gerstein M (2000) The morph server: A standardized system for analyzing and visualizing macromolecular motions in a database framework. *Nucleic Acids Res* 28:1665–1675.